APL Materials

Investigating the spin-orbit interaction in van der Waals heterostructures by means of the spin relaxation anisotropy

Cite as: APL Mater. **7**, 120701 (2019); https://doi.org/10.1063/1.5124894
Submitted: 18 August 2019 . Accepted: 20 November 2019 . Published Online: 10 December 2019

L. Antonio Benítez, Juan F. Sierra, Williams Savero Torres, Matias Timmermans, Marius V. Costache, and Sergio O. Valenzuela

Investigating the spin-orbit interaction in van der Waals heterostructures by means of the spin relaxation anisotropy

Cite as: APL Mater. 7, 120701 (2019); doi: 10.1063/1.5124894
Submitted: 18 August 2019 • Accepted: 20 November 2019 •
Published Online: 10 December 2019

L. Antonio Benítez,[1,2,a] Juan F. Sierra,[1,b] Williams Savero Torres,[1] Matias Timmermans,[1] Marius V. Costache,[1] and Sergio O. Valenzuela[1,3,c]

AFFILIATIONS

[1]Catalan Institute of Nanoscience and Nanotechnology (ICN2), CSIC and BIST, Campus UAB, Bellaterra 08193, Barcelona, Spain
[2]Universitat Autònoma de Barcelona, Bellaterra 08193, Barcelona, Spain
[3]ICREA—Institució Catalana de Recerca i Estudis Avançats, 08010 Barcelona, Spain

[a)]an.benitez7@gmail.com
[b)]juan.sierra@icn2.cat
[c)]SOV@icrea.cat

ABSTRACT

Graphene offers long spin propagation and, at the same time, a versatile platform to engineer its physical properties. Proximity-induced phenomena, taking advantage of materials with large spin-orbit coupling or that are magnetic, can be used to imprint graphene with large spin-orbit coupling and magnetic correlations. However, full understanding of the proximitized graphene and the consequences on the spin transport dynamics requires the development of unconventional experimental approaches. The investigation of the spin relaxation anisotropy, defined as the ratio of lifetimes for spins pointing out of and in the graphene plane, is an important step in this direction. This review discusses various methods for extracting the spin relaxation anisotropy in graphene-based devices. Within the experimental framework, current understanding on spin transport dynamics in single-layer and bilayer graphene is presented. Due to increasing interest, experimental results in graphene in proximity with high spin-orbit layered materials are also reviewed.

I. INTRODUCTION

Two-dimensional (2D) materials are envisioned as fundamental building blocks for next generation nanoelectronic devices, offering promising prospects and a vast number of potential applications.[1] Among 2D materials, graphene, a material made of carbon atoms arranged in a honeycomb lattice, is particularly relevant due to its structural stability and superior electronic properties.[2,3] Graphene is also promising for spin-based devices in which the electron spin degree of freedom, as opposed to its charge, plays a central role.[4,5] The weak intrinsic spin-orbit coupling (SOC) in graphene (12 μeV) and the lack of hyperfine interaction (99% of ^{12}C nuclei in which the nuclear spin is zero) ensure that spins propagate coherently through the crystal lattice over long distances.[6–8] Such an intrinsic property has motivated many experimental and theoretical studies over the last ten years. Early numerical calculations by Ertler *et al.*[9] showed spin lifetimes between micro- and milliseconds for single-layer graphene, in stark contrast with the first experimental observation of 100 ps.[10] Since then, experimental efforts have focused on improving the quality of the devices and then enhancing the spin relaxation parameters. Substrate effects in spin transport were suppressed by suspending graphene, resulting in spin relaxation lengths of up to 5 μm while spin relaxation times stayed in the 100 s picosecond range.[11,12] Subsequently, hexagonal boron nitride (hBN) was used to fully encapsulate graphene, resulting in spin lifetimes exceeding 10 ns, but still orders of magnitude below original predictions.[13]

Recent theoretical models attribute the short experimental spin lifetimes to spin-pseudospin entanglement driven by SOC or to resonant scattering by local magnetic moments.[6,14–18] The spin lifetime anisotropy, ζ, a parameter that quantifies the ratio between spin lifetimes for spins lying in the graphene plane ($\tau_s^{\parallel}$) and pointing out of it ($\tau_s^{\perp}$), can help discriminate between these relaxation mechanisms. In particular, ζ is highly sensitive to the magnitude and orientation of existing spin-orbit fields (SOFs), if they drive the spin relaxation. For instance, for SOFs oriented in the graphene plane derived from Rashba SOC, out-of-plane spins relax faster leading to $\tau_s^{\perp} < \tau_s^{\parallel}$, i.e., $\zeta < 1$.[9,19] The relation is expected to change to $\tau_s^{\perp} > \tau_s^{\parallel}$, and consequently, $\zeta > 1$ for spin relaxation driven by flexural distortions.[20] When there is no preferential direction in the spin relaxation, as in the case of spin relaxation driven by paramagnetic impurities or (random) gauge fields, the relaxation becomes isotropic with $\tau_s^{\perp} = \tau_s^{\parallel}$, so $\zeta = 1$.[15,16] Given that the SOFs in graphene can be altered using compounds with large SOC, spin-relaxation anisotropy is a crucial parameter to investigate spin-orbit proximity effects.

The aim of this Research Update is to provide a comprehensive overview of the current experimental progress toward understanding spin relaxation phenomena in graphene-based devices by means of spin relaxation anisotropy experiments. The presented experimental methods are general and can, in principle, be applied to other systems, such as transition metal dichalcogenides (TMDCs), phosphorene, germanene, or silicene, as long as the corresponding spin relaxation lengths allow the fabrication of suitable devices. This manuscript first introduces the general concept of spin injection and detection in lateral spin devices, followed by a detailed explanation of the different methods allowing the determination of the spin relaxation anisotropy. Within this framework, recent experiments are reviewed on single-layer and bilayer graphene as well as on graphene-based heterostructures. Finally, future experiments to further advance the understanding of spin related phenomena in these systems are discussed.

II. SPIN INJECTION AND DETECTION IN GRAPHENE LATERAL DEVICES

A. Nonlocal detection technique

Spin transport properties in graphene are typically studied in lateral devices using nonlocal techniques. The basic concept dates back to 1985 when Johnson and Silsbee experimentally demonstrated that an unequal density of spin-up and spin-down electrons can be generated and detected in nonmagnetic materials using ferromagnets.[21,22] A typical graphene-based lateral spin device consists of four electrodes lithographically designed on top of graphene [see Fig. 1(a)]. The inner electrodes (F1 and F2) act as the spin injector and spin detector, respectively, and are made of ferromagnetic metals (F), typically Co. The distance L between F1 and F2 defines the spin channel length. The outer electrodes (M1, M2) are ideally made of a nonmagnetic metal so that they do not participate in spin injection and detection.[23] A resistive (tunnel) barrier is introduced between the F metal electrode and the graphene channel. This barrier prevents the carriers from losing their spin information and enhances the spin polarization.[24,25] Typical barriers include thin oxide layers such as AlO_x, MgO, TiO_x, or SrO,[10,26–28] layered dielectrics such as hBN,[29,30] and amorphous carbon layers or fluorinated graphene.[31,32] Generally, graphene lateral spin devices are fabricated on an insulating layer on a highly conducting substrate (e.g., SiO_2 or hBN on p-doped Si). The graphene carrier density n can then be controlled by applying a back-gate voltage between the graphene and the conducting substrate.

In the nonlocal scheme, a current source I is applied between the electrodes F1 and M1. Because of the spin-splitting of the bands in F1, the injected current is spin-polarized, creating a spin accumulation underneath the contact. This nonequilibrium spin density diffuses along the spin channel toward the detector electrode F2. The magnitude of the local spin accumulation at the F2 position is quantified by measuring the voltage drop V_{nl} between F2 and M2.[23] An external magnetic field B applied along the easy-axis of the ferromagnets controls the relative orientation of F1 and F2. A typical nonlocal measurement, shown in Fig. 1(b), presents sharp transitions that

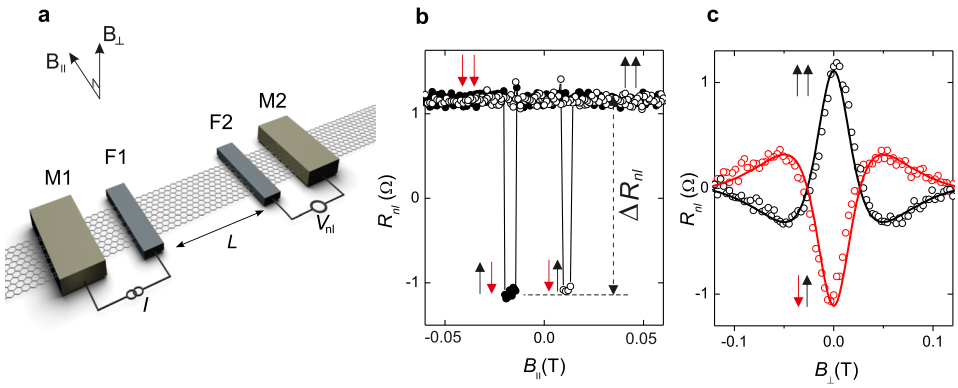

FIG. 1. (a) Schematics of a graphene lateral spin device with spin-sensitive electrodes acting as the spin injector (F1) and spin detector (F2). (b) Typical nonlocal spin resistance R_{nl} as a function of the in-plane magnetic field B applied along the easy-axis of F1 and F2. The sharp transitions from positive to negative R_{nl} mark the switching from the parallel to antiparallel configurations between F1 and F2, as illustrated by the arrows. (c) Spin precession measurements for the parallel and antiparallel alignment of F1 and F2 magnetizations (symbols). Solid lines correspond to the fitting to Eq. (1) that allows the extraction of the spin dependent parameters. For the shown example, $\tau_s^{\parallel} = 0.21$ ns, $D_s = 0.012$ m^2 s^{-1}, and $\lambda_s^{\parallel} = 1.58$ μm.

indicate the change from the parallel to antiparallel configurations of the F1 and F2 magnetizations. The difference in V_{nl} between the parallel and the antiparallel configurations, $\Delta V_{nl} = V_{nl}^{\uparrow\uparrow} - V_{nl}^{\uparrow\downarrow}$, is the nonlocal spin signal, which is commonly expressed in terms of resistance units as $\Delta R_{nl} = \Delta V_{nl}/I$.[23]

B. Spin precession experiments

Information about the spin relaxation length and the spin lifetime is typically obtained by means of (Hanle) spin precession experiments. Here, a magnetic field $B_\perp$ is applied perpendicular to the substrate causing an in-plane spin precession as spins diffuse from F1 to F2.[21,33] The shape of a typical Hanle spin precession curve in the high contact resistance limit is given by the expression

$$R_{nl}(B) = \pm\frac{P_i P_d}{e^2 NA}\int_0^\infty \frac{1}{\sqrt{4\pi D_s t}}\exp\left[-\frac{L^2}{4D_s t}\right] \times \cos(\omega_L t)\exp(-t/\tau_s^{\parallel})dt, \quad (1)$$

where the + (−) sign accounts for the parallel (antiparallel) configuration of the injector and detector, and P_i and P_d, e, N, and A are the spin polarization of the injector and the detector, the electron charge, the density of states at the Fermi energy, and the contact area, respectively. D_s and $\tau_s^{\parallel}$ stand for the spin diffusion constant and the spin lifetime while $\lambda_s^{\parallel} = \sqrt{D_s\tau_s^{\parallel}}$ is the spin relaxation length. The Larmor frequency is given by $\omega_L = \gamma_c B_\perp$, with $\gamma_c = g\mu_B/\hbar$, where g is the gyromagnetic factor, μ_B the Bohr magneton, and $\hbar$ is the reduced Planck constant. The spin projection over the detector is captured in the term $\cos(\omega_L t)$, whereas $\frac{1}{\sqrt{4\pi D_s t}}\exp\left[-\frac{L^2}{4D_s t}\right]$ is the probability that the injected spins reach the detector at a time t and $\exp(-t/\tau_s^{\parallel})$ represents the effect of spin relaxation. Spin precession measurements for the parallel and antiparallel configurations are shown in Fig. 1(c). The spin signal is maximum at $B = 0$, and its absolute value decreases with increasing B and vanishes at large magnetic fields due to spin dephasing; $\tau_s^{\parallel}$, D_s, and $\lambda_s^{\parallel}$ are extracted by fitting the Hanle curve to Eq. (1).

Until 2016, most experiments used the configuration described above to determine spin relaxation properties, with the magnetic field applied perpendicular to the substrate. In this situation, spins precess in the plane of the spin channel, and, therefore, $\tau_s^{\parallel}$ and $\lambda_s^{\parallel}$ are actually the spin lifetime and spin relaxation length for spins oriented *in-plane* (thus, the $\parallel$ symbol). As discussed in Sec. III, Raes *et al.* demonstrated that the application of oblique magnetic fields[34] or, alternatively, in-plane magnetic fields perpendicular to the magnetizations of F1 and F2[35] enables the determination of the spin lifetime $\tau_s^{\perp}$ and spin relaxation lengths $\lambda_s^{\perp}$ for spins oriented *out-of-plane*. The simplicity of this experimental approach combined with its lack of artifacts has led to an increasing number of theoretical and experimental studies to investigate the spin relaxation anisotropy and gather information on spin relaxation mechanisms and SOC.

III. DETERMINATION OF THE SPIN-LIFETIME ANISOTROPY

The magnetization of the F electrodes on a typical device [Fig. 1(a)] is oriented in-plane along their long axis due to magnetic shape anisotropy. Therefore, spins are injected in the plane of the channel. The first reported method to determine the spin lifetime anisotropy in graphene uses a large $B_\perp$ (>1 T) to tilt the magnetization of the F electrodes along the field direction in order to enable the injection of spins perpendicular to the graphene plane. The spin lifetime anisotropy ζ is then extracted by comparing the spin signals when the injected spins are oriented in plane ($B_\perp = 0$) and perpendicular to it ($B_\perp > 1$ T). The disadvantage of extracting ζ with this method arises from the large magnetoresistive effects that are present in graphene, which limits its range of validity to sufficiently large carrier concentrations n.[36] Therefore, alternative experimental approaches have been developed, which produce out-of-plane spin populations by spin precession and require much lower magnetic fields. Raes *et al.* discussed two such approaches under an oblique magnetic field[34] or under a magnetic field applied in the graphene plane and perpendicular to the F metal electrodes.[35] They focused on the oblique case because the large rotation of the F electrodes magnetizations for in-plane fields generally complicates the data analysis and increases the uncertainty in the determination of ζ.[35] Shortly afterwards, Ghiasi *et al.*[37] and Benítez *et al.*[38] implemented anisotropy measurements with in-plane magnetic fields in graphene modified by proximity of a TMDC, where the anisotropy is so large that it can still be readily visualized and quantified. In Subsections III A and III B, the characteristics of these methods are discussed in detail.

A. Oblique spin precession

1. Homogeneous spin channel

A schematic of the oblique spin precession method is shown in Fig. 2(a). The magnetic field B, characterized by the angle β, is applied in a plane that contains the F metal electrode long axis and is perpendicular to the substrate. The spin density $\vec{s}$ under an oblique magnetic field satisfies the one-dimensional steady state Bloch equation,

$$D_s\nabla^2\vec{s} - \gamma_c\vec{s}\times\vec{B} - \overline{\tau_s^{-1}}\cdot\vec{s} = 0, \quad (2)$$

where D_s is the spin diffusion constant and $\overline{\tau_s^{-1}}$ is a 3 × 3 tensor with entries $\tau_s^{\parallel}$ and $\tau_s^{\perp}$.

The simplest approach to solve Eq. (2) is to transform the coordinates (e^x, e^y, e^z) into the rotated Cartesian axis system characterized by unit vectors (e^x, $e^{B^\parallel}$, $e^{B^\perp}$). In the new coordinate system, the applied magnetic field $\vec{B} = (0, B, 0)$ can only induce precession to the spin population $\vec{s} = (s^x, s^{B^\parallel}, s^{B^\perp})$ perpendicular to it. The solution of Eq. (2) for a homogeneous spin channel is described in detail in Ref. 35. Refined models include contact-induced spin relaxation due to the finite contact resistance[39] and inhomogeneous spin lifetimes in the graphene channel.[37,38]

The solution of Eq. (2) for different values of ζ with B oriented at $\beta = 45°$ is shown in Fig. 3(a). It is observed that at $B \equiv B_d \sim 70$ mT, the spin component perpendicular to B is fully dephased. For $B > B_d$, the precessional motion is completely suppressed, and thus, R_{nl} saturates to the remanent nonprecessional spin component that lies along the magnetic field direction. In this situation, R_{nl} at the F detector is given by $R_{nl}^{\beta} = \overline{R}_{nl}(\zeta,\beta)\cos^2(\beta^*)$,

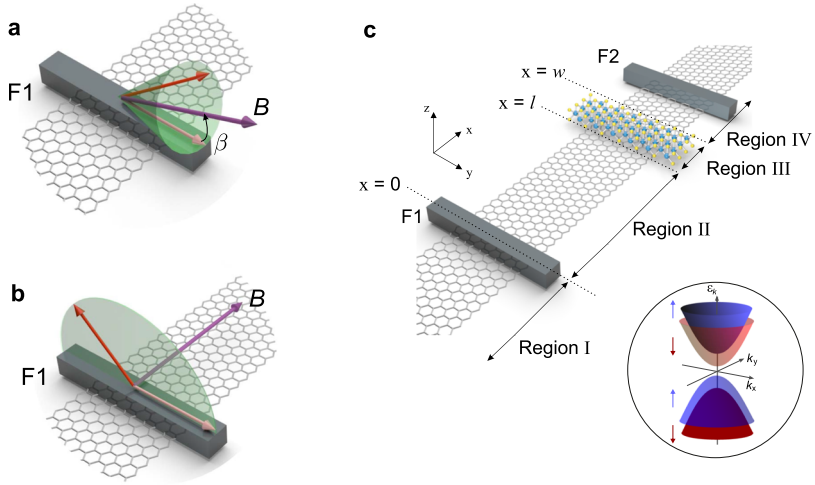

FIG. 2. Determination of the spin relaxation anisotropy ratio ζ by means of spin precession. (a) Schematics of the oblique spin precession method. The magnetic field B is applied at an angle β in a plane that contains the easy-axis of the ferromagnetic injector (F1) and that is perpendicular to the substrate. (b) Schematics of the out-of-plane spin precession method. The magnetic field B is applied in plane and perpendicular to the easy-axis of the ferromagnetic injector (F1). (c) Illustration of a graphene-based lateral spin device with a nonhomogeneous spin channel. Regions I, II, and IV indicate the pristine graphene channel while region III is covered with a TMDC. As a spin diffuses from F1 to F2 under an oblique (a) or in-plane (b) magnetic field, it undergoes precession. As it approaches the TMDC, it gathers an out-of-plane component. Inset in (c) represents the graphene electronic band structure close to the Dirac point for graphene/TMDC. The colors and arrows represent the out-of-plane spin sub-bands. ε_k and $K_{x,y}$ account for the energy band and the wave vectors respectively.

where $\beta^* = \beta - \gamma(\beta, B)$ takes into consideration the tilting angle $\gamma(\beta, B)$ of the magnetization of the F electrodes that results from the applied magnetic field, as calculated below. The factor $\cos^2(\beta^*)$ accounts for the projection of the injected spins along the magnetic field direction and the subsequent projection along the easy-axis of the F detector. The term $\overline{R}_{\rm nl}(\zeta, \beta)$ is given by[34]

$$\overline{R}_{\rm nl}(\zeta,\beta) = \sqrt{f(\zeta,\beta)}\exp\left[-\frac{L}{\lambda_s^{\parallel}}\left(\sqrt{\frac{1}{f(\zeta,\beta)}}-1\right)\right]R_{\rm nl}^0. \quad (3)$$

In this expression, $f(\zeta,\beta) = \left(\cos^2(\beta) + \frac{1}{\zeta}\sin^2(\beta)\right)^{-1}$ and $R_{\rm nl}^0$ is the value of the nonlocal resistance at $B = 0$. For the isotropic case, it is

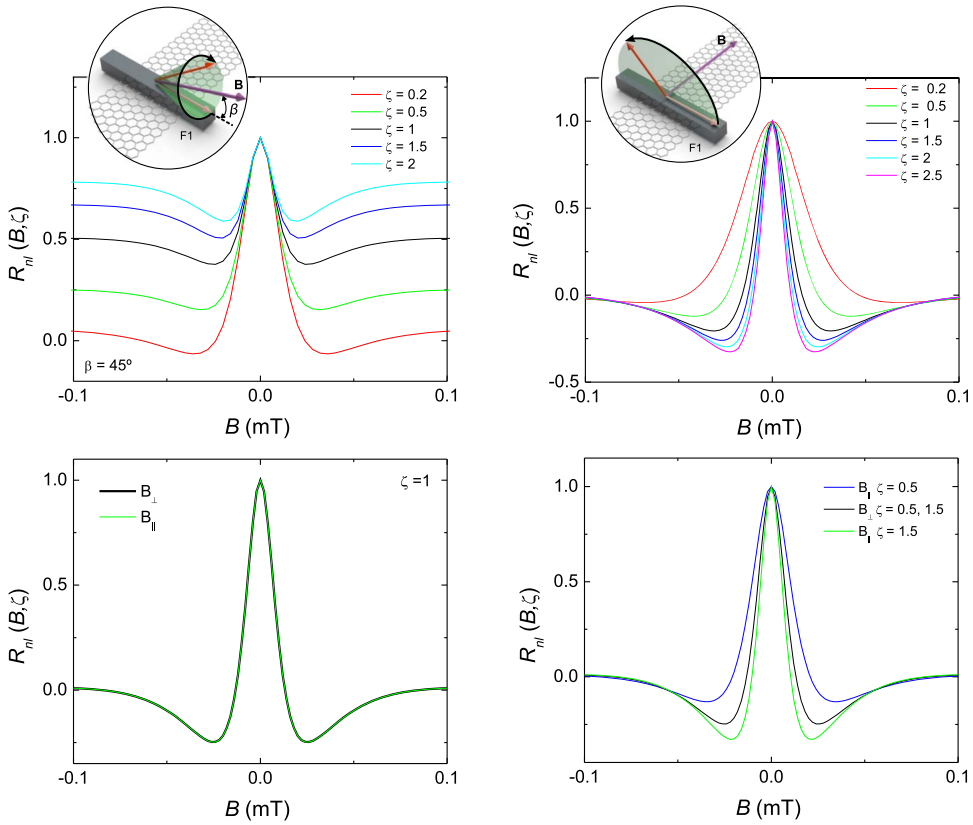

FIG. 3. Spin precession line shapes $R_{\rm nl}(B, \zeta)$ obtained numerically using Eq. (2) in an anisotropic medium. (a) $R_{\rm nl}(B, \zeta)$ for the oblique spin precession method at fixed $\beta = 45°$ for anisotropy ratios $\zeta = 0.2$, 0.5, 1.5, and 2. The dashed line corresponds to the isotropic case ($\zeta = 1$). As ζ increases, the asymptotic value of the spin signal increases. (b) Numerically extracted spin precession line shapes $R_{\rm nl}(B, \zeta)$ for the out-of-plane spin precession method for anisotropy ratios $\zeta = 0.2$, 0.5, 1.5, 2, and 2.5. The dashed line corresponds to the isotropic case ($\zeta = 1$). As ζ decreases, the position of the minima shifts to higher magnetic fields. $R_{\rm nl}(B, \zeta)$ for magnetic fields applied out of plane ($B_\perp$) and in plane ($B_\parallel$) for the isotropic (c) and anisotropic (d) cases. The perfect overlap between the two curves in (c) is a consequence of the isotropic spin relaxation, while in (d), the difference between $R_{\rm nl}$ for $B_\perp$ and $B_\parallel$ allows us to easily identify the anisotropy nature of the spin transport. All the curves are normalized to their value at $B = 0$ and are obtained for $L = 7$ μm, $D_s = 0.02$ m^2 s^{-1}. The in-plane spin lifetime is constant in all curves, $\tau_s^{\parallel} = 0.5$ ns, and only $\tau_s^{\perp}$ is changed.

straightforward to verify that $\overline{R}_{\rm nl}(\zeta = 1, \beta)$ is independent of β and its value corresponds to $\overline{R}_{\rm nl}(\zeta = 1, \beta) = R^0_{\rm nl}$.

The tilt angle γ of the F electrodes magnetizations can be calculated by considering the Stoner-Wohlfarth model, which provides a good approximation for a coherent magnetization rotation at low B. The relationship between γ and β is given by the expression[40]

$$\gamma = \arcsin\left[\frac{B\sin(\beta)}{B_s + B\cos(\beta)}\right], \tag{4}$$

where B_s is the saturation magnetic field. In the specific case of $\beta = 90^\circ$, $\gamma = \arcsin(B/B_s)$. The functional dependence of γ with B is followed closely by experimental results on anisotropic magnetoresistance and Hanle spin precession experiments, from which B_s is readily obtained.[34]

A fundamental design parameter to correctly determine ζ using Eq. (3) is the spin channel length L. In particular, a minimum L is required to observe complete dephasing of the spin component perpendicular to the magnetic field at sufficiently low B, typically $B_d \lesssim 0.15$ T, thus avoiding magnetoresistance effects. Considering no contact effects in the spin relaxation process, the contribution to the spin signal stemming from the spin component perpendicular to the magnetic field $R^{\perp}_{nl}$ can be written as $R^{\perp}_{nl}(B) \propto \exp(-L((B\gamma_c/2D_s)^{1/2} - 1/(D_s\tau^{\parallel}_s)^{1/2}))$.[39] Defining a threshold value for the saturation such that $R^{sat}_{nl} = 10^{-\eta}R_{\rm nl}(B = 0)$, the condition $R^{\perp}_{nl}(B_d) \leq R^{sat}_{nl}$ establishes that $L \geq \sqrt{\frac{2D_s}{B_d\gamma_c}}\,\eta \ln 10$. Assuming high-quality devices with $\lambda_s = 30\ \mu$m, $D_s = 0.075$ m^2 s^{-1}, and a saturation threshold $10^{-\eta} = 10^{-3}$,[13,39] the minimum channel length is $L \approx 16\ \mu$m to achieve full dephasing at $B_d = 0.15$ T.

2. Inhomogeneous spin channel

In the case of a nonuniform spin channel, Eqs. (1) and (3) are no longer valid to obtain the spin related parameters and ζ. This is particularly relevant for heterostructures comprising graphene with other materials covering partially the spin channel [see Fig. 2(c)]. Here, the diffusive process is governed by Eq. (2) with boundary conditions,

$$\begin{aligned} &x = 0 : \vec{s}_{\rm I} = \vec{s}_{\rm II};\ \partial_x\vec{s}_{\rm I} - \partial_x\vec{s}_{\rm II} = \vec{s}_0 \\ &x = l : \vec{s}_{\rm II} = \vec{s}_{\rm III};\ \partial_x\vec{s}_{\rm II} = \partial_x\vec{s}_{\rm III} \\ &x = w : \vec{s}_{\rm III} = \vec{s}_{\rm IV};\ \partial_x\vec{s}_{\rm III} = \partial_x\vec{s}_{\rm IV} \\ &x \to \pm\infty : \vec{s} = 0, \end{aligned} \tag{5}$$

where I, II, and IV denote the pristine graphene and III the heterostructure region. Spins are injected in the y direction $\vec{s}_0 = (0, s_0, 0)$, where s_0 is a constant that depends on the injected electrical current and the contact polarization. Spin absorption effects are not taken into account.

B. Out-of-plane spin precession

A schematic of the out-of-plane spin precession method is shown in Fig. 2(b). Here, the magnetic field B is applied in plane and in a direction perpendicular to the easy-axis of the F metal electrodes. The precession occurs in a plane perpendicular to the substrate containing the easy axis, thus probing both $\tau^{\perp}_s$ and $\tau^{\parallel}_s$. The solution of Eq. (2) for this configuration is shown in Fig. 3(b). For $\zeta \gg 1$, $R_{\rm nl}$ strongly deviates from the isotropic case $\zeta = 1$; therefore, a large anisotropy can be easily identified.[37,38,41] The magnitude of the minimum in $R_{\rm nl}$ corresponds to an average spin rotation angle of $\pm\pi$. When B increases, spins start to acquire an out-of-plane component, which relaxes slower than the in plane one when $\zeta > 1$. Then, for an average spin rotation of $\pm\pi$ and $\zeta \gg 1$, $R_{\rm nl}$ can be larger than its value at $B = 0$ (when spins are always in plane and the spin lifetime is short). In contrast, for $\zeta < 1$, the out-of-plane spin component relaxes faster than the in-plane one, implying that the minimum in $R_{\rm nl}$ is less pronounced and can eventually disappear for $\zeta \ll 1$.

In addition, Fig. 3(b) shows that the position of the minima, which occurs for a collective π spin precession, changes with ζ. A spin contributes a precession angle ϕ in a diffusion time t with a probability $P(t)$ such that $t = \phi/\omega_L$. Here, $P(t)$ is determined by the product of the diffusion-time distribution function and the probability that the spin has *not* flipped during t. The latter is proportional to $\exp(-t/\tau_s)$, resulting in a suppressed probability at long t or, equivalently, at large ϕ. Such a suppression is more significant for short spin lifetimes, which implies that the collective spin precession angle for a given B will increase with longer spin lifetimes. This explains why the minima in Fig. 3(b) develop at lower B as ζ increases.[35] Figure 3(c) compares $R_{\rm nl}$ when B is applied in-plane ($B_{\parallel}$, out-of-plane spin precession) and out-of-plane ($B_{\perp}$, in-plane spin precession) for the isotropic case $\zeta = 1$, where no differences are observed between the two configurations. These results are in stark contrast to those when $\zeta \neq 1$. In this case, $R_{\rm nl}$ clearly depends on the magnetic field orientation, as shown in Fig. 3(d). For out-of-plane spin precession, $R_{\rm nl}$ lies above (below) the in-plane spin precession line shape when $\zeta > 1$ ($\zeta < 1$). Comparing the in-plane and out-of-plane spin precession curves is a straightforward way to check the isotropic/anisotropic character of the system.

IV. SPIN RELAXATION ANISOTROPY EXPERIMENTS IN LATERAL SPIN DEVICES

Having introduced the fundamental tools to determine the spin lifetime anisotropy, this section first overviews recent implementations in single- and bilayer graphene lateral spin devices. Then, it introduces graphene-based heterostructures in which the graphene SOC is enhanced by proximity of a high spin-orbit material, in particular, in van der Waals heterostructures formed by graphene and TMDCs.

A. Spin relaxation anisotropy in single-layer graphene

The first experimental efforts to extract ζ in graphene lateral spin devices required the application of out-of-plane magnetic fields, as described in Sec III. The magnitude of the spin signal was found to be smaller for out-of-plane spin injection than for in-plane spin injection. Tombros *et al.*[42] reported $\zeta \sim 0.8$ with $\tau^{\parallel}_s = 60$ ps for graphene on SiO_2. A similar approach was later used by Guimarães *et al.*[36] in graphene fully encapsulated with hBN with enhanced spin relaxation times $\tau^{\parallel}_s = 2$ ns and higher carrier mobilities. Double encapsulation with hBN enables the control of the electric field E and the carrier density n independently by applying top- and back-gate voltages. The values of ζ were reported to be electric-field tunable, with $\zeta \sim 0.75$ for $E = 0$ V/nm to $\zeta \sim 0.65$ for $E = 0.7$ V/nm.

However, the determination of $\tau^{\perp}_s$ with perpendicularly magnetized electrodes requires the use of intense magnetic fields,

which represents a major drawback stemming from magnetoresistive effects. The graphene layer resistance and associated diffusion constant are magnetic-field dependent, reducing the range of carrier densities in which the method can be applied. These effects are more pronounced close to the charge neutrality point (CNP) and in samples with large carrier mobilities;[43] in such a scenario, they have to be taken into consideration even at moderate applied magnetic fields. Figure 4(a) shows the squared resistance R_{sq} of graphene as a function of $B_\perp$ for different n (back-gate voltages V_g). As expected, magnetoresistance is largest nearby the CNP, with variations in R_{sq} in excess to 35% at $B \approx 1$ T. For B below ~0.2 T, the variations are less than 3%, independently of V_g [see the inset in Fig. 4(a)]. Figure 4(b) shows spin precession measurements with the magnetic field applied out-of-plane. It shows that R_{nl} increases for $B > 0.5$ T because of the out-of-plane rotation of the electrodes' magnetization. As B increases, a saturation of R_{nl} is expected when the rotation is completed. However, further increase in B shows that R_{nl} presents a monotonous decrease after reaching a maximum value at $B \sim 1.5$ T. This behavior is observed even far from the CNP and can be partially explained by a suppressed spin injection and detection efficiency due to the increased graphene resistance. Following the analysis reported in Refs. 36 and 42, for a signal decrease of 45% and 70%, as displayed in Fig. 4(b), $\zeta = 0.55$ and $\zeta = 0.3$, respectively. This result differs from the actual $\zeta \sim 1$ extracted with the oblique spin precession method in the same device at low magnetic fields [Fig. 5(b)].

Figure 5 shows typical spin precession measurements for a representative set of β values for graphene onto two different substrates, SiO_2[34] and hBN. In both cases, $\tau_s^{\parallel}$ is between 0.2 ns and 0.4 ns. When applying the oblique precession method (Sec. III A), the precessional motion is suppressed at $B_d \sim 0.1$ T for all β and the remanent nonlocal spin signal is independent of B. The remanent signal derives from the nonprecessing spin component that lies along the B direction, whose magnitude R_{nl}^{β} depends on β as expected from Eq. (3). Figures 5(b) and 5(d) show R_{nl} above B_d [marked by a vertical line in Figs. 5(a) and 5(c)] normalized to 1, $R_{nl}^{\beta}/R_{nl}^{0}$, as a function of $\cos^2(\beta^*)$. From Eq. (3), for the isotropic case, i.e., $\zeta = 1$, $R_{nl}^{\beta}/R_{nl}^{0} = \cos^2(\beta^*)$ so $R_{nl}^{\beta}/R_{nl}^{0}$ as a function of $\cos^2(\beta^*)$ results in a straight line with slope equal to one. For the anisotropic case, $R_{nl}^{\beta}/R_{nl}^{0}$ lies above the straight line ($\zeta > 1$) or below it ($\zeta < 1$), as extracted from Eq. (3). For both SiO_2 and hBN substrates, experimental results are in excellent agreement with $\zeta \sim 1$, and thus, $\tau_s^{\parallel} = \tau_s^{\perp}$ which is independent of n. A more recent experiment in low-mobility CVD graphene on SiO_2 by Ringer *et al.*[44] combines the oblique and out-of-plane spin precession experiments to extract ζ, yielding $\zeta \sim 0.9$–0.7, with $\tau_s^{\parallel}$ between 1.1 ns and 0.7 ns. Nevertheless, measurements as a function of n and temperature in highest quality graphene devices and a careful analysis of the F magnetization with B in plane are still necessary.

Initially, models based on the Elliot-Yafet (EY) and Dyakonov-Perel (DP) mechanisms were adopted to explain spin relaxation in graphene. In the EY mechanism, the spin relaxation arises from spin flips between scattering events leading to a linear scaling between the momentum relaxation time τ_p and $\tau_s^{\parallel}$. In the DP mechanism, spins precess around an effective SOF between scattering events leading to a scaling $\tau_p \propto \tau_s^{\parallel -1}$.[6] While the EY and DP mechanisms have successfully explained spin relaxation in metals and semiconductors, experiments in graphene attempting to discriminate between them have yielded contradictory results; reports searching for scaling laws between τ_p and $\tau_s^{\parallel}$ suggested spin relaxation consistent with EY, DP, or a combination of both.[45–48] Nevertheless, several conclusions can be drawn from the spin lifetime anisotropy results. For DP mechanisms with Rashba SOFs, $\zeta = 0.5$ is expected, while for EY driven by phonon scattering, $\zeta \approx 0$;[6] therefore, they cannot explain $\zeta = 1$ on their own. The presence of resonant scattering by local magnetic moments, arising from adatoms or vacancies, could explain the experimental results. Calculations considering sp^3 bonded hydrogen adatoms can account for the observed spin lifetimes even for very small hydrogen concentration (~1 ppm).[15,16,18] The paramagnetic nature of the local magnetic moments results in a random spin orientation after each scattering event, so $\zeta = 1$. Additionally, the common features observed in the case of single-layer graphene independently of the type of substrate (Fig. 5) suggest that the substrate plays a minor role in making the spin relaxation isotropic, at least for graphene with moderate mobility.

B. Spin relaxation anisotropy in bilayer graphene

Besides high mobilities at room temperature, gate-tunable carrier density, and parabolic bands near the K and K' points, bilayer graphene offers the possibility to tune the bandgap with a transverse

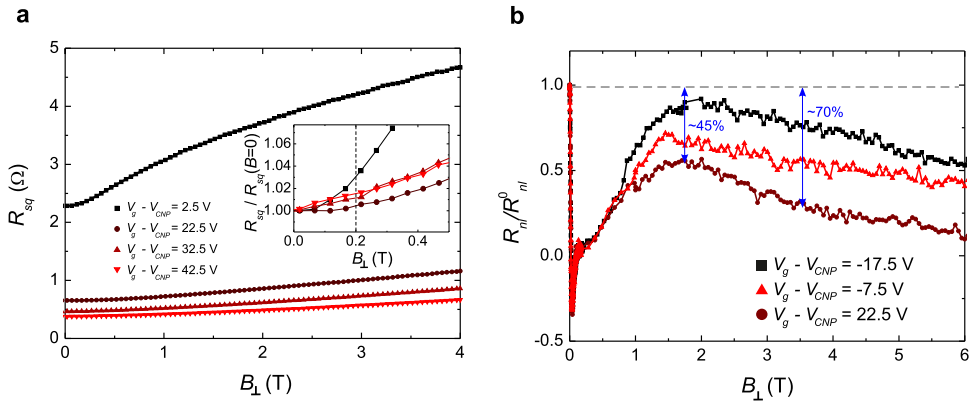

FIG. 4. (a) Graphene squared resistance R_{sq} for different back-gates V_g as a function of the applied out-of-plane magnetic field $B_\perp$. (Inset) Normalized R_{sq} at low values of $B_\perp$. The dashed line marks the limit of $B_\perp$ where the oblique spin precession measurements are typically carried out. (b) Spin precession measurements at high magnetic fields for different V_g. The blue arrows mark the signal difference between $B = 0$, $B_\perp = 1.5$ T, and $B_\perp = 3.5$ T. Reproduced with permission from Raes *et al.*, Nat. Commun. **7**, 11444 (2016). Copyright 2016 Springer Nature.

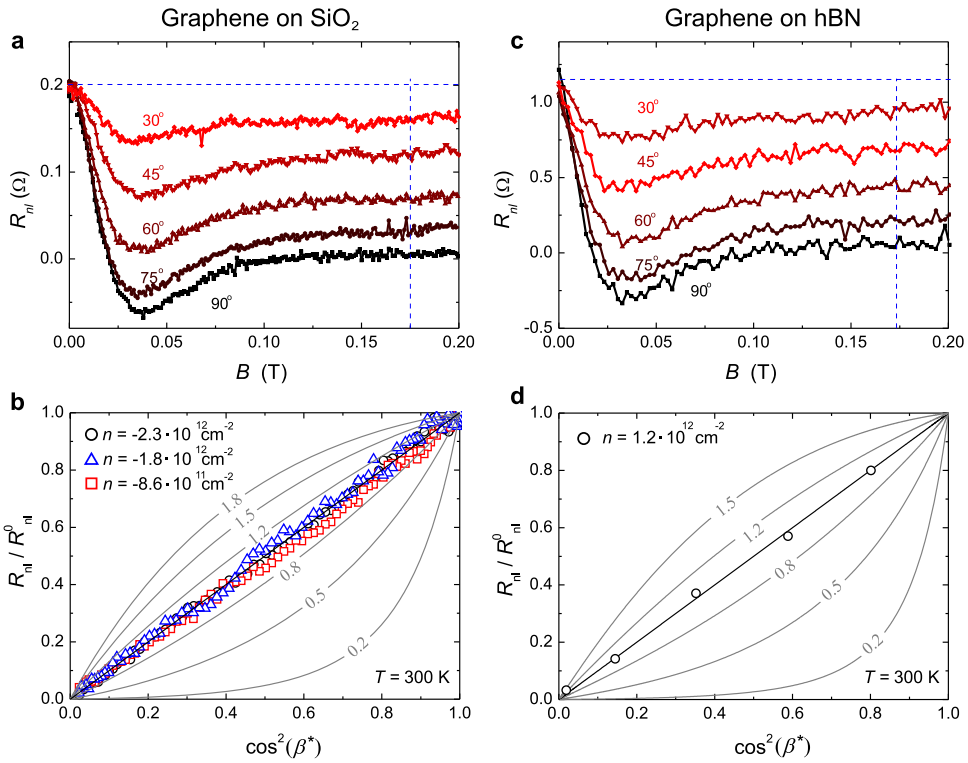

FIG. 5. Room temperature spin precession measurements acquired for the parallel magnetization configuration of the spin injector and detector for oblique magnetic fields B applied at different angles β (from 90° to 30°) in single-layer graphene on SiO_2 (a) and hBN (c). The carrier densities are $n = -2.3 \times 10^{12}$ cm^{-2} and $n = 1.2 \times 10^{12}$ cm^{-2}, respectively. R_{nl} normalized by $R_{nl,0}$ vs $\cos^2\beta^*$ for the SiO_2 (b) and hBN (d). The solid lines in (b) and (d) represent R_{nl} for the indicated value of ζ calculated with Eq. (3), and the black straight line corresponds to the isotropic case, $\zeta = 1$. [(a) and (b)] Reproduced with permission from Raes *et al.*, Nat. Commun. **7**, 11444 (2016). Copyright 2016 Springer Nature.

electric field.[49,50] First principles calculations show that the intrinsic SOC around the K and K' is about 12 μeV and points out of the bilayer graphene plane, similar to single-layer graphene.[49] The space inversion symmetry breaking, caused by the substrate or an external electric field, results in an extrinsic Bychkov-Rashba SOC pointing in-plane that removes the spin and valley degeneracy. The Bychkov-Rashba SOC increases with the carrier density n, whereas the intrinsic SOC decreases with n. Thus, spin relaxation driven by SOC can be inferred from ζ.

Spin relaxation anisotropy measurements using the oblique spin precession method have been recently reported in bilayer graphene encapsulated with hBN.[41,51] Leutenantsmeyer *et al.*[51] demonstrated that ζ can be large and tunable at low temperatures (75 K). By controlling the carrier concentration n with a back-gate voltage applied to the insulating substrate, ζ was found to vary from 3.5 at $n = 6 \times 10^{11}$ cm^{-2} to about 8 at the CNP [Fig. 6(a)]. Because ζ is larger close to the CNP, the driven spin relaxation anisotropy is attributed to the intrinsic out-of-plane spin orbit fields that induce a significant spin-valley coupling.[51] Similar results in dual-gate devices were independently observed by Xu *et al.*[41] The use of a global back-gate and a local top-gate allowed them to control the carrier density and the transverse electric field. A value of $\zeta = 12$ is extracted at low temperatures (100 K) near the CNP under a transverse electric field $E = -0.5$ V/nm [Fig. 6(b)]. In addition, Xu

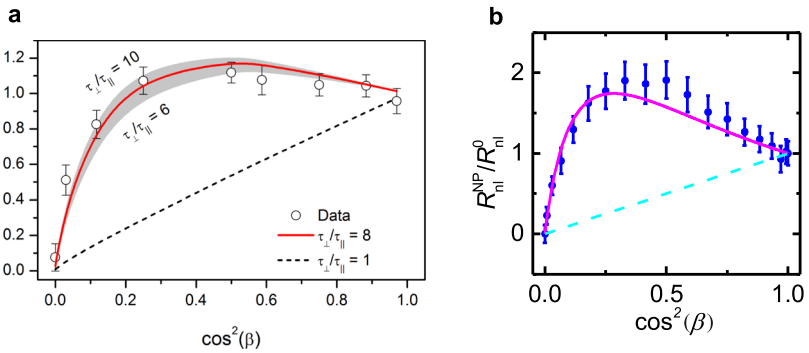

FIG. 6. Spin anisotropy experiments in bilayer graphene. (a) R_{nl} normalized by $R_{nl,0}$ vs $\cos^2\beta$ close to the CNP of fully encapsulated bilayer graphene.[51] (b) Spin anisotropic behavior in the presence of a transverse electric field $E = -0.5$ V/nm and close to the charge neutrality point (CNP) in dual-gate devices.[41] (a) Reproduced with permission from Leutenantsmeyer *et al.*, Phys. Rev. Lett. **121**, 127702 (2018). Copyright 2018 American Physical Society, (b) reproduced with permission from Xu *et al.*, Phys. Rev. Lett. **121**, 127703 (2018). Copyright 2018 American Physical Society.

et al. observed isotropic behavior for $n \geq 4 \times 10^{12}$ cm^{-2}. Temperature dependent measurements show a decrease in ζ, resulting in isotropic behavior at room temperature. Besides the highly tunable value of the spin lifetime anisotropy, $\tau_s^{\parallel}$ is about 10 ns, two orders of magnitude larger than those observed in van der Waals heterostructures with similar values of ζ (Sec. IV C), which can be ascribed to the larger SOC in the latter.

C. Spin relaxation anisotropy in single-layer graphene/TMDC heterostructures

Emerging graphene-based spintronics applications, such as spin-logic devices, require tunability of a large SOC via electric fields. Although not accessible in pristine graphene, this can be achieved by stacking graphene with high spin-orbit materials. Layered semiconducting TMDCs, which comprise heavy transition

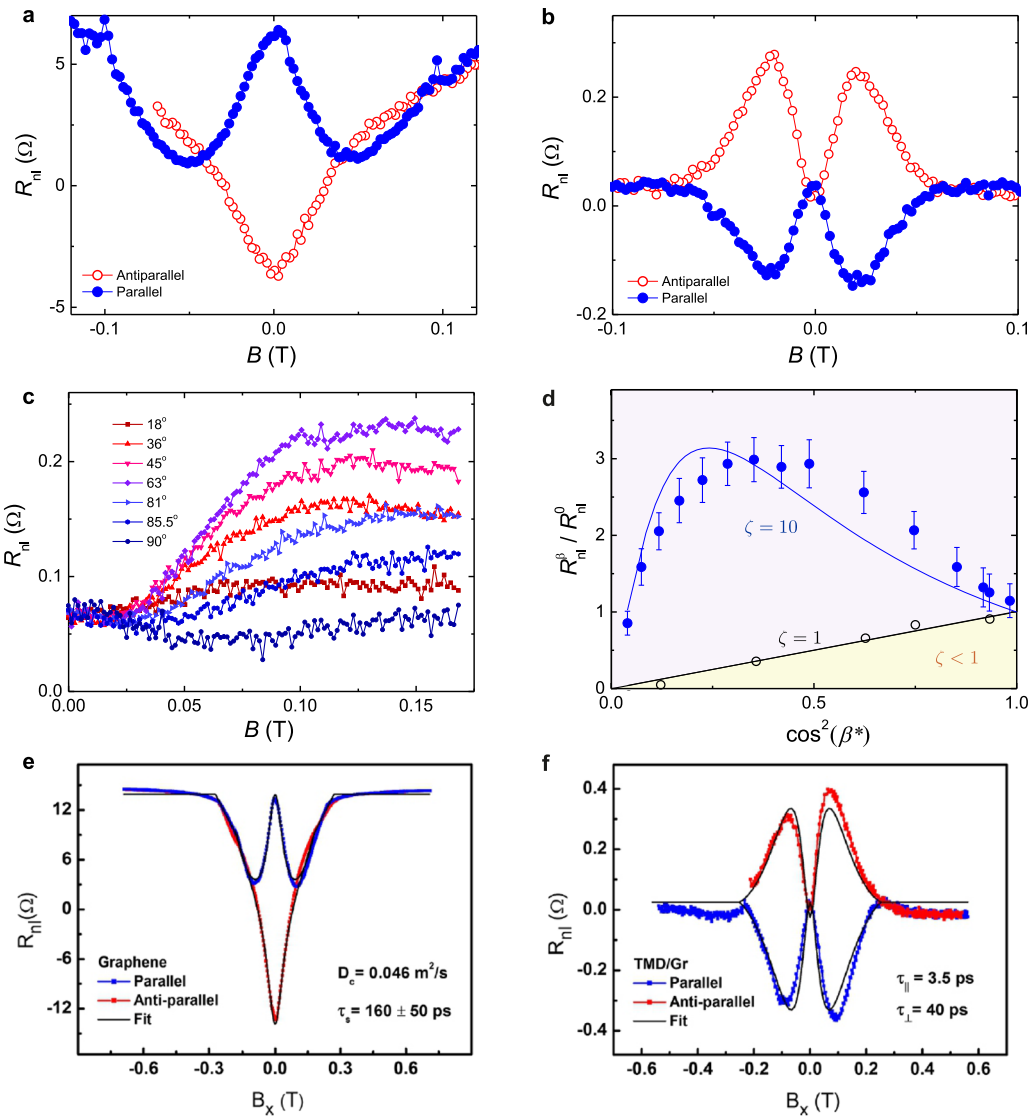

FIG. 7. Spin anisotropy experiments in lateral spin devices comprising single-layer graphene and a transition metal dichalcogenide (TMDC). [(a), (b), (e), and (f)] The out-of-plane spin precession method with an in-plane magnetic field (B_x). [(a) and (e)] Spin precession in homogeneous single-layer graphene reference devices. [(b) and (f)] Spin precession in nonhomogeneous devices with a single-layer graphene channel partially covered with WS_2 (b) at room temperature and $MoSe_2$ (f) at 75 K. (c) Room temperature spin precession curves obtained by the oblique precession method at the indicated β in a graphene/WS_2 device. The precession curves correspond to the parallel magnetization configuration of the spin injector and detector. Full dephasing of the precessing component is observed at $B > 0.12$ T. (d) R_{nl} normalized by R_{nl}^0 vs $\cos^2(\beta^*)$. The data represented by full symbols are extracted from (c) at $B = 0.16$ T. The solid blue line represents the modeled response for $\zeta = 10$. The data represented by open symbols correspond to the reference device with $\zeta = 1$ in (a). [(a)–(d)] Reproduced with permission from Benítez *et al.*, Nat. Phys. **14**, 303 (2018). Copyright 2018 Springer Nature. [(e) and (f)] Reproduced with permission from Ghiasi *et al.*, Nano Lett. **17**, 7528 (2017). Copyright 2017 American Chemical Society.

metal atoms (such as Mo or W) and chalcogen atoms (such as S, Se, or Te), are of special relevance. First principles calculations have shown a proximity-induced enhancement of the SOC in graphene by TMDCs in the millielectron-volt range.[52] When graphene is in proximity with a TMDC, it preserves its linear Dirac band structure and a bandgap opens due to broken pseudospin symmetry, while the proximity-induced SOC and broken space inversion symmetry remove the spin degeneracy and lead to a strong spin-valley coupling[53] [see schematics in the inset of Fig. 2(c)]. About the K and K' points, spins have an out of plane component, alternating from up to down as the energy of the bands increases, and a winding in-plane component, as a consequence of the Rashba-type SOC. The out-of-plane spins and in-plane texture reverse the sign between the K and K' points.[52] Such spin texture has a direct impact on the spin dynamics, leading to distinct spin lifetimes $\tau_s^{\parallel}$ and $\tau_s^{\perp}$.

Weak (anti)localization measurements have been commonly used to evidence SOC enhancement in graphene/TMDC.[54–57] In such experiments, spin-orbit scattering times are extracted from quantum corrections to the magnetoconductivity, the most notable signature being a decrease in the spin lifetime to the picosecond range. However, it is not straightforward to distinguish between the influence of symmetric and antisymmetric spin-orbit scattering times, which are related to the in-plane and out-of-plane spin relaxation times.[54,58] In addition, weak (anti)location measurements are restricted to low temperatures (typically bellow 10 K), which makes the method limited in comparison to spin precession experiments (see Sec. III).

Spin precession experiments on graphene/TMDC heterostructures use a lateral spin device geometry schematically shown in Fig. 2(c). It consists of a nonhomogeneous spin channel in which single-layer graphene is partially covered with a TMDC. Spins are injected through F1 and diffuse along the graphene channel toward F2. Due to the proximity-induced SOC in the graphene/TMDC region, the in-plane and out-of-plane spins have different associated lifetimes.

Experiments carried out by Ghiasi *et al.*[37] in graphene/$MoSe_2$ heterostructures at low temperatures (75 K) and by Benítez *et al.*[38] in graphene/WS_2 (and MoS_2) heterostructures at room temperature have demonstrated strongly anisotropic spin transport behavior. Figures 7(a) and 7(b) summarize the features of the spin precession response in the out-of-plane precession configuration [Fig. 2(b)] in single-layer graphene and when WS_2 is placed over the graphene spin channel.[38] For isotropic spin relaxation in graphene [Fig. 7(a)], R_{nl} has its highest value at $B = 0$ and starts decreasing with B due to spin precession and dephasing. At sufficiently large B, the magnetization of the F electrodes rotates and eventually saturates along the field direction. As injected spins are parallel to B, they do not precess any longer and R_{nl} recovers its value at $B = 0$. This is in stark contrast with the features observed in the graphene/TMDC heterostructure [Fig. 7(b)]. As B increases, R_{nl} becomes much larger than its value at $B = 0$. The maximum magnitude of R_{nl} is reached when the diffusing spins rotate $\sim\pi/2$ at the TMDC location and point roughly out of plane. The subsequent decrease in R_{nl} is due to spin dephasing and the rotation of the magnetization of the F contacts. The anomalous enhancement of R_{nl} is a clear indication of anisotropic spin relaxation, with $\lambda_s^{\perp} > \lambda_s^{\parallel}$ and thus $\zeta \gg 1$. Figure 7(c) further shows R_{nl} for different β using the oblique spin precession configuration. The strongly anisotropic behavior is manifested in R_{nl} normalized to $R_{nl}(B = 0)$ vs $\cos^2(\beta^*)$ [Fig. 7(d)]. Results similar to those in Figs. 7(a) and 7(b) have been independently observed in graphene/$MoSe_2$ at $T = 75$ K [Figs. 7(e) and 7(f)].[37] The reported values for $\tau_s^{\parallel}$ and $\tau_s^{\perp}$ are 3–3.5 ps and 30–40 ps, respectively, with $\zeta \sim 10$, for both graphene/$MoSe_2$ and graphene/WS_2. The experimental values of $\tau_s^{\parallel}$ and $\tau_s^{\perp}$ are well reproduced by numerical simulations and microscopic theories of spin relaxation anisotropy that consider a strong intervalley scattering in the graphene/TMDC heterostructure.[59,60] Intervalley scattering arises from short-range elastic scattering centers, e.g., structural defects in graphene or vacancies in the TMDC. Due to the strong spin-valley coupling present in graphene/TMDC heterostructures, the out-plane spin relaxation follows the Dyakonov-Perel mechanism with the out-plane spin relaxation rate controlled by the momentum scattering time (τ_p), i.e., $1/\tau_s^{\perp} \propto \tau_p$, while the in-plane spin relaxation is dominated by the intervalley scattering time (τ_{iv}), i.e., $1/\tau_s^{\parallel} \propto \tau_{iv}$. With strong intervalley scattering, $\tau_{iv} \ll \tau_p$, the spin lifetime anisotropy ζ extracted from numerical simulations lies between 20 and 200, with $\tau_s^{\parallel} \sim 1$ ps and $\tau_s^{\perp} \sim 20$–100 ps, which agrees well with the experimental results.

V. CONCLUSIONS AND PERSPECTIVES

This Research Update describes the state-of-the-art techniques to determine the spin lifetime anisotropy in lateral spin devices. The so-called oblique and out-of-plane spin precession methods are considered the most reliable. Their development has motivated a growing interest in evaluating anisotropic spin dynamics, by modeling and experiments, as a means of gathering information about graphene intrinsic SOC and about proximity-induced SOC in van der Waals heterostructures. The discussed experiments represent the starting point of this lively research area that aims at investigating new physical phenomena and novel spintronics applications using 2D materials.

Future experiments will aim at identifying intrinsic spin relaxation in graphene, without the presence of dominant magnetic scattering centers, and at achieving full control of the spin dynamics by manipulating the SOC with external electric fields. Spin relaxation anisotropy must be studied in ultraclean devices with large mobilities.[13] Encapsulating graphene with a top hBN dielectric could protect graphene from chemicals and aggressive device fabrication processes, which can introduce adatoms or impurities acting as magnetic scattering centers.[61] Such *extrinsic* contributions can actively mask or alter the *intrinsic* spin-relaxation processes. On the other hand, recent first-principles calculations predict a giant spin relaxation anisotropy in graphene on hBN depending on the stacking configuration and external electric fields,[62] which has not been implemented in the experiments so far.

The case of graphene-based heterostructures is of special relevance because they can play a key role in the development of spin logics and novel devices based on coupled spin-valley dynamics. Spin lifetime anisotropy experiments are consistent with proximity-induced SOC and intervalley scattering as the origin of the spin relaxation. However, the experimentally extracted values are somewhat smaller than those obtained by numerical simulations. In this regard, high interface quality of graphene with other high spin-orbit layered materials is essential to ultimately control the

magnitude of the induced SOC by the action of external electric fields.

Finally, the investigation of spin relaxation anisotropy is inherently related to spin-charge conversion (SCC), as both phenomena derive from SOC characteristics.[63] In recent years, there has been a growing interest in observing proximity-induced SCC in graphene/TMDC heterostructures.[63–66] Very recently, Benítez *et al.* have unambiguously demonstrated tunable proximity-induced spin Hall and spin galvanic effects in graphene/WS_2.[63] Notably, the experiments have shown the existence of large spin relaxation anisotropy in the structure, raising questions regarding our current understanding of the origin of the SOC[67–69] and demonstrating that the combined study of SCC and spin relaxation anisotropy is essential for further understanding these fascinating systems.[70,71]

ACKNOWLEDGMENTS

This research was supported by the European Union's Horizon 2020 research and innovation programme Graphene Flagship Core 1 and 2 under Grant Agreement Nos. 696656 and 785219, respectively, by the European Research Council under grant agreement 306652 SPINBOUND, by the Spanish Ministry of Economy and Competitiveness, MINECO (Grant Nos. MAT2016-75952-R and SEV-2017-0706 Severo Ochoa), and by the CERCA Programme and the Secretariat for Universities and Research, Knowledge Department of the Generalitat de Catalunya 2017 SGR 827.

REFERENCES

[1] G. Fiori, F. Bonaccorso, G. Iannaccone, T. Palacios, D. Neumaier, A. Seabugh, S. Banarjee, and L. Colombo, Nat. Nanotechnol. **9**, 768 (2014).
[2] A. H. Castro Neto, F. Guinea, N. M. R. Peres, K. S. Novoselov, and A. K. Geim, Rev. Mod. Phys. **81**, 109 (2009).
[3] S. Das Sarma, S. Adam, E. H. Hwang, and E. Rossi, Rev. Mod. Phys. **83**, 407 (2011).
[4] I. Žutić, J. Fabian, and S. Das Sarma, Rev. Mod. Phys. **76**, 323 (2004).
[5] A. Fert, Rev. Mod. Phys. **80**, 1517 (2008).
[6] W. Han, R. K. Kawakami, M. Gmitra, and J. Fabian, Nat. Nanotechnol. **9**, 794 (2014).
[7] Z. M. Gebeyehu, S. Parui, J. F. Sierra, M. Timmermans, M. J. Esplandiu, S. Brems, C. Huyghebaert, K. Garello, M. V. Costache, and S. O. Valenzuela, 2D Mater. **6**, 034003 (2019).
[8] M. V. Kamalakar, C. Groenveld, A. Dankert, and S. P. Dash, Nat. Commun. **6**, 6766 (2015).
[9] C. Ertler, S. Konschuh, M. Gmitra, and J. Fabian, Phys. Rev. B **80**, 041405 (2009).
[10] N. Tombros, C. Jozsa, M. Popinciuc, H. T. Jonkman, and B. J. van Wees, Nature **448**, 571 (2007).
[11] I. Neumann, J. Van de Vondel, G. Bridoux, M. V. Costache, F. Alzina, C. M. S. Torres, and S. O. Valenzuela, Small **9**, 156 (2013).
[12] M. H. D. Guimarães, A. Veligura, P. J. Zomer, T. Maassen, I. J. Vera-Marun, N. Tombros, and B. J. van Wees, Nano Lett. **12**, 3512 (2012).
[13] M. Drögeler, C. Franzen, F. Volmer, T. Pohlmann, L. Banszerus, M. Wolter, K. Watanabe, T. Taniguchi, C. Stampfer, and B. Beschoten, Nano Lett. **16**, 3533 (2016).
[14] S. Roche and S. O. Valenzuela, J. Phys. D: Appl. Phys. **47**, 094011 (2014).
[15] D. Kochan, M. Gmitra, and J. Fabian, Phys. Rev. Lett. **112**, 116602 (2014).
[16] D. Soriano, D. V. Tuan, S. M.-M. Dubois, M. Gmitra, A. W. Cummings, D. Kochan, F. Ortmann, J.-C. Charlier, J. Fabian, and S. Roche, 2D Mater. **2**, 022002 (2015).
[17] S. Roche, J. Åkerman, B. Beschoten, J.-C. Charlier, M. Chshiev, S. P. Dash, B. Dlubak, J. Fabian, A. Fert, M. Guimarães, F. Guinea, I. Grigorieva, C. Schönenberger, P. Seneor, C. Stampfer, S. O. Valenzuela, X. Waintal, and B. van Wees, 2D Mater. **2**, 030202 (2015).
[18] D. Kochan, S. Irmer, M. Gmitra, and J. Fabian, Phys. Rev. Lett. **115**, 196601 (2015).
[19] D. Huertas-Hernando, F. Guinea, and A. Brataas, Phys. Rev. Lett. **103**, 146801 (2009).
[20] S. Fratini, D. Gosálbez-Martínez, P. Merodio Cámara, and J. Fernández-Rossier, Phys. Rev. B **88**, 115426 (2013).
[21] M. Johnson and R. H. Silsbee, Phys. Rev. Lett. **55**, 1790 (1985).
[22] M. Johnson and R. H. Silsbee, Phys. Rev. B **37**, 5326 (1988).
[23] S. O. Valenzuela, Int. J. Mod. Phys. B **23**, 2413 (2009).
[24] E. I. Rashba, Phys. Rev. B **62**, R16267 (2000).
[25] G. Schmidt, D. Ferrand, L. W. Molenkamp, A. T. Filip, and B. J. van Wees, Phys. Rev. B **62**, R4790 (2000).
[26] W. Han, K. Pi, K. M. McCreary, Y. Li, J. J. I. Wong, A. G. Swartz, and R. K. Kawakami, Phys. Rev. Lett. **105**, 167202 (2010).
[27] J. F. Sierra, I. Neumann, J. Cuppens, B. Raes, M. V. Costache, and S. O. Valenzuela, Nat. Nanotechnol. **13**, 107 (2018).
[28] S. Singh, J. Katoch, T. Zhu, R. J. Wu, A. S. Ahmed, W. Amamou, D. Wang, K. A. Mkhoyan, and R. K. Kawakami, Nano Lett. **17**, 7578 (2017).
[29] M. V. Kamalakar, A. Dankert, J. Bergsten, T. Ive, and S. P. Dash, Sci. Rep. **4**, 6146 (2014).
[30] M. Gurram, S. Omar, and B. J. van Wees, Nat. Commun. **8**, 248 (2017).
[31] I. Neumann, M. V. Costache, G. Bridoux, J. F. Sierra, and S. O. Valenzuela, Appl. Phys. Lett. **103**, 112401 (2013).
[32] C. H. Li, J. T. Robinson, and B. T. Jonker, Nature Commun. **5**, 3161 (2014).
[33] F. J. Jedema, H. B. Heersche, A. T. Filip, J. J. A. Baselmans, and B. J. van Wees, Nature **416**, 713 (2002).
[34] B. Raes, J. E. Scheerder, M. V. Costache, F. Bonell, J. F. Sierra, J. Cuppens, J. Van de Vondel, and S. O. Valenzuela, Nat. Commun. **7**, 11444 (2016).
[35] B. Raes, A. W. Cummings, F. Bonell, M. V. Costache, J. F. Sierra, S. Roche, and S. O. Valenzuela, Phys. Rev. B **95**, 085403 (2017).
[36] M. H. D. Guimarães, P. J. Zomer, J. Ingla-Aynés, J. C. Brant, N. Tombros, and B. J. van Wees, Phys. Rev. Lett. **113**, 086602 (2014).
[37] T. S. Ghiasi, J. Ingla-Aynés, A. A. Kaverzin, and B. J. van Wees, Nano Lett. **17**, 7528 (2017).
[38] L. A. Benítez, J. F. Sierra, W. Savero Torres, A. Arrighi, F. Bonell, M. V. Costache, and S. O. Valenzuela, Nat. Phys. **14**, 303 (2018).
[39] T. Zhu and R. K. Kawakami, Phys. Rev. B **97**, 144413 (2018).
[40] S. Blundell, *Magnetism in Condensed Matter* (Oxford University Press, USA, 2001).
[41] J. Xu, T. Zhu, Y. K. Luo, Y.-M. Lu, and R. K. Kawakami, Phys. Rev. Lett. **121**, 127703 (2018).
[42] N. Tombros, S. Tanabe, A. Veligura, C. Jozsa, M. Popinciuc, H. T. Jonkman, and B. J. van Wees, Phys. Rev. Lett. **101**, 046601 (2008).
[43] S. Cho and M. S. Fuhrer, Phys. Rev. B **77**, 081402 (2008).
[44] S. Ringer, S. Hartl, M. Rosenauer, T. Völkl, M. Kadur, F. Hopperdietzel, D. Weiss, and J. Eroms, Phys. Rev. B **97**, 205439 (2018).
[45] W. Han and R. K. Kawakami, Phys. Rev. Lett. **107**, 047207 (2011).
[46] C. Józsa, T. Maassen, M. Popinciuc, P. J. Zomer, A. Veligura, H. T. Jonkman, and B. J. van Wees, Phys. Rev. B **80**, 241403 (2009).
[47] F. Volmer, M. Drögeler, E. Maynicke, N. von den Driesch, M. L. Boschen, G. Güntherodt, and B. Beschoten, Phys. Rev. B **88**, 161405 (2013).
[48] P. J. Zomer, M. H. D. Guimarães, N. Tombros, and B. J. van Wees, Phys. Rev. B **86**, 161416 (2012).
[49] E. McCann and M. Koshino, Rep. Prog. Phys. **76**, 056503 (2013).
[50] S. Konschuh, M. Gmitra, D. Kochan, and J. Fabian, Phys. Rev. B **85**, 115423 (2012).
[51] J. C. Leutenantsmeyer, J. Ingla-Aynés, J. Fabian, and B. J. van Wees, Phys. Rev. Lett. **121**, 127702 (2018).
[52] M. Gmitra and J. Fabian, Phys. Rev. B **92**, 155403 (2015).

[53]D. Xiao, G.-B. Liu, W. Feng, X. Xu, and W. Yao, Phys. Rev. Lett. **108**, 196802 (2012).
[54]S. Zihlmann, A. W. Cummings, J. H. Garcia, M. Kedves, K. Watanabe, T. Taniguchi, C. Schönenberger, and P. Makk, Phys. Rev. B **97**, 075434 (2018).
[55]T. Wakamura, F. Reale, P. Palczynski, S. Guéron, C. Mattevi, and H. Bouchiat, Phys. Rev. Lett. **120**, 106802 (2018).
[56]T. Wakamura, F. Reale, P. Palczynski, M. Q. Zhao, A. T. C. Johnson, S. Guéron, C. Mattevi, A. Ouerghi, and H. Bouchiat, Phys. Rev. B **99**, 245402 (2019).
[57]T. Völkl, T. Rockinger, M. Drienovsky, K. Watanabe, T. Taniguchi, D. Weiss, and J. Eroms, Phys. Rev. B **96**, 125405 (2017).
[58]E. McCann and V. I. Fal'ko, Phys. Rev. Lett. **108**, 166606 (2012); e-print arXiv:1111.5267.
[59]A. W. Cummings, J. H. Garcia, J. Fabian, and S. Roche, Phys. Rev. Lett. **119**, 206601 (2017).
[60]M. Offidani and A. Ferreira, Phys. Rev. B **98**, 245408 (2018).
[61]M. Wojtaszek, I. J. Vera-Marun, T. Maassen, and B. J. van Wees, Phys. Rev. B **87**, 081402 (2013).
[62]K. Zollner, M. Gmitra, and J. Fabian, Phys. Rev. B **99**, 125151 (2019).
[63]L. A. Benítez, W. S. Torres, J. F. Sierra, M. Timmermans, J. H. Garcia, S. Roche, M. V. Costache, and S. O. Valenzuela, Nat. Mater. (to be published); e-print arXiv:1908.07868 (2019).
[64]A. Avsar, J. Y. Tan, T. Taychatanapat, J. Balakrishnan, G. Koon, Y. Yeo, J. Lahiri, A. Carvalho, A. S. Rodin, E. O'Farrell, G. Eda, A. H. Castro Neto, and B. Özyilmaz, Nat. Commun. **5**, 4875 (2014).
[65]C. K. Safeer, J. Ingla-Aynés, F. Herling, J. H. Garcia, M. Vila, N. Ontoso, M. R. Calvo, S. Roche, L. E. Hueso, and F. Casanova, Nano Lett. **19**, 1074 (2019).
[66]T. S. Ghiasi, A. A. Kaverzin, P. J. Blah, and B. J. van Wees, Nano Lett. **19**, 5959 (2019).
[67]J. H. Garcia, A. W. Cummings, and S. Roche, Nano Lett. **17**, 5078 (2017).
[68]M. Offidani, M. Milletarì, R. Raimondi, and A. Ferreira, Phys. Rev. Lett. **119**, 196801 (2017).
[69]Y.-H. Lin, M. Offidani, C. Huang, M. A. Cazalilla, and A. Ferreira, e-print arXiv:1906.10448 (2019).
[70]J. Sinova, S. O. Valenzuela, J. Wunderlich, C. H. Back, and T. Jungwirth, Rev. Mod. Phys. **87**, 1213 (2015).
[71]D. Van Tuan, J. M. Marmolejo-Tejada, X. Waintal, B. K. Nikolić, S. O. Valenzuela, and S. Roche, Phys. Rev. Lett. **117**, 176602 (2016).